

# ESTIMATION OF NOISE SHIELDING EFFECT OF NEXT-GENERATION AIRCRAFT BY A COMPUTATIONAL AEROACOUSTICS METHOD

Yuma Fukushima\*

\*Department of Aerospace Engineering, Tohoku University  
 fukushima@edge.ifs.tohoku.ac.jp

**Keywords:** *Noise, Silent aircraft, Computational Aeroacoustics*

## Abstract

*Noise shielding effect of an Over-the-Wing-mounted-Nacelle (OWN) configuration was estimated. The Linearized Euler Equation code for aeroacoustic analysis has been developed on block-structured Cartesian mesh to treat the complicated geometries robustly and accurately. In the present method, high-order schemes are used for the spatial derivation and time integration, and the immersed boundary method based on the ghost cell approach is employed at the wall boundary. At the block boundary between neighboring blocks, higher-order data exchange is conducted with Lagrange interpolation, while outgoing wave is damped by absorbing boundary domain near the outer boundary. The results show that the far-field SPL of OWN configuration is lower than that of the conventional Under-the-Wing-mounted-Nacelle configuration by about 10dB due to the shielding effect of the OWN configuration.*

## 1 Introduction

Green aviation adjusting to the noise regulation for the next generation has been proposed and intensively studied by Japan Aerospace Exploration Agency (JAXA), National Aeronautics and Space Administration (NASA), research institutes of European countries and so on. To satisfy the severe requirements of environmental-friendly aircraft, great technological advances are needed to the conventional aircraft. Presently, some of the most remarkable targets are noise, emission and

fuel consumption. For example, NASA sets the aggressive target values for the three requirements for next-generation aircrafts [1]. Figure 1 shows the average noise level of commercial aircraft, noise regulation set by International Civil Aviation Organization (ICAO) and the target values of “N+1” and “N+2” concepts of NASA’s project. From the figure, it is clear that the continual reduction of noise has been realized steadily for about forty years mainly due to the improvement of engine performance. There are, for example, the increase of bypass ratio, the use of geared fan machinery and the improvement of liners and vanes. Figure 1 also shows that the noise regulations of airport noise are getting stringent. Aircrafts of the next generation must meet these regulations and also have margins for tougher limits.

Noise from aircrafts is categorized into two main groups, airframe noise and engine noise. Airframe noise is mainly turbulent sound generated from high-lift devices and landing gears. Engine noise is the sum of fan and jet noise. During takeoff, fan and jet noise are dominant because the engine is at full throttle. On the other hand, the airframe and fan noise are dominant at the landing. In each scene, fan noise is one of the most dominant factors of noise from aircrafts. To realize the dramatic noise reduction of the engine noise, shielding the noise from engine nacelle by fuselage or wings is one of reasonable approaches. From this point of view, various unique aircrafts have been proposed and researched in numerical and experimental approaches for the future direction. To design such unconventional aircrafts, it is

important to analyze the noise propagation and estimate the shielding effect accurately. However, experimental approach is expensive in general, and it is difficult to estimate the far-field noise directivity. In the recent progress of computer performance, it is getting possible to simulate the noise generation, reflection or diffraction by aircraft and the propagation to far-field by numerical approach.

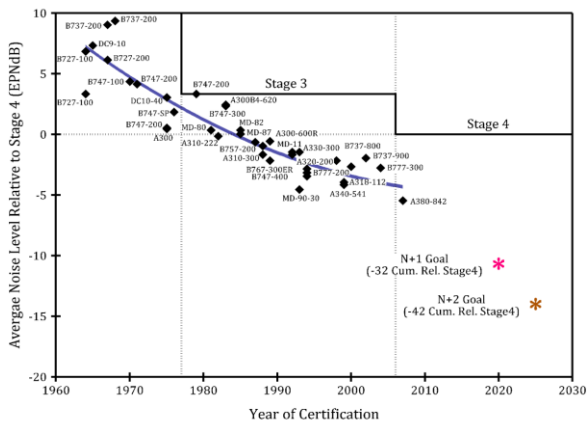


**Fig. 1. Change in commercial noise level as function of time (Ref. 1)**

The major numerical approach of aeroacoustics simulation is Aerodynamic/Acoustic splitting method. Flow field around sound source is initially calculated by Computational Fluid Dynamics (CFD) simulation. Acoustic field is then estimated from the physical quantities of flow field. In this strategy, the method using Curle's equation is superior in terms of computational cost. However, the method assumes the compactness condition which means the flow is uniform and sound source is small compared to the distance to the observing points. These assumptions are not satisfied to the analysis of real airplane noise. Another general way is the computation based on the Linearized Euler Equation (LEE) which is one of the accurate methods capturing the propagation of sound. The method is used to analyze noise propagation from axisymmetric engine. LEE calculation can deal with noise propagation from non-compact sound sources in non-uniform mean flow. It can also treat diffraction and reflection near the object.

LEE is often calculated on structured or unstructured meshes. From the practical point of view, these meshes have some problems in analysis of realistic complicated geometries. Structured mesh is fitted to geometry and is able to treat the detailed components precisely, but mesh generation around whole airplane or more complicated geometries is quite difficult and time-consuming. Unstructured mesh is applicable to complicated geometries, but generally low-order accuracy in space. High-order unstructured method takes much computational cost and thus not practical at the moment. Following these problems, simple Cartesian mesh is focused in this research. Generation of Cartesian mesh is based on simple orthogonal division of computational domain and thus it can treat complicated geometries easily. Furthermore, high-order scheme is easily applied by the extension of stencils. Rapid computation is achieved from the simple computational structure on the Cartesian mesh. The problem of Cartesian mesh is numerical error caused by staircase surface representation. In this research, locally refined mesh and Immersed Boundary Method (IBM) are applied to solve the problem. IBM is the method proposed to treat curved objects accurately. This helps to maintain practical mesh spacing required for reasonable timestep of explicit method and highly-accurate wall boundary representation. Analysis with Cartesian mesh requires finer mesh near objects to reduce the error of staircase surface representation. However, it is difficult to control local mesh size on conventional simple Cartesian mesh. Therefore, block-structured, Cartesian mesh method, the Building-Cube Method (BCM) [2], [3], is employed in this research. Using this method, meshes which have appropriate resolution can be locally assigned in computational domain.

The main purpose of this study is to simulate noise scattering around DLR-F6 and Over-the-Wing-mounted-Nacelle (OWN) configuration. And the noise shielding effect of OWN is estimated as a realistic computation around complicated geometries. To achieve the purpose, block-structured Cartesian mesh of BCM with IBM for wall boundary condition is employed.

## 2 Numerical Method

### 2.1 Linearized Euler Equation

The governing equations of the three-dimensional LEE are represented in Eqs. (1) and (2). It can be said that LEEs are wave equation with advective and input term, and these are sufficient equations to calculate the realistic sound propagation. At the calculation of LEEs, average components of flow field,  $Q_0$  and sound source,  $S$  are inputted. Then, the time evolution of fluctuation component  $Q'$  is computed.

$$\frac{\partial Q'}{\partial t} + \frac{\partial E}{\partial x} + \frac{\partial F}{\partial y} + \frac{\partial G}{\partial z} + H = S \quad (1)$$

$$Q' = \begin{bmatrix} \rho' \\ u' \\ v' \\ w' \\ p' \end{bmatrix} \quad E = \begin{bmatrix} \rho_0 u' + \rho' u_0 \\ u_0 u' + \frac{p'}{\rho_0} \\ u_0 v' \\ u_0 w' \\ u_0 p' + \gamma p_0 u' \end{bmatrix}$$

$$F = \begin{bmatrix} \rho_0 v' + \rho' v_0 \\ v_0 u' \\ v_0 v' + \frac{p'}{\rho_0} \\ v_0 w' \\ v_0 p' + \gamma p_0 v' \end{bmatrix} \quad G = \begin{bmatrix} \rho_0 w' + \rho' w_0 \\ w_0 u' \\ w_0 v' \\ w_0 w' + \frac{p'}{\rho_0} \\ w_0 p' + \gamma p_0 w' \end{bmatrix} \quad (2)$$

$$H = \begin{bmatrix} 0 \\ u' \left( \frac{\partial u_0}{\partial x} - \nabla \cdot \bar{\mathbf{v}}_0 \right) + \frac{1}{(\rho_0)^2} \left( \rho' \frac{\partial p_0}{\partial x} + p' \frac{\partial \rho_0}{\partial x} \right) \\ v' \left( \frac{\partial v_0}{\partial y} - \nabla \cdot \bar{\mathbf{v}}_0 \right) + \frac{1}{(\rho_0)^2} \left( \rho' \frac{\partial p_0}{\partial y} + p' \frac{\partial \rho_0}{\partial y} \right) \\ w' \left( \frac{\partial w_0}{\partial z} - \nabla \cdot \bar{\mathbf{v}}_0 \right) + \frac{1}{(\rho_0)^2} \left( \rho' \frac{\partial p_0}{\partial z} + p' \frac{\partial \rho_0}{\partial z} \right) \\ (\gamma - 1) \left[ p' \nabla \cdot \bar{\mathbf{v}}_0 - \bar{\mathbf{v}} \cdot \nabla p_0 \right] \end{bmatrix}$$

The governing equations are nondimensionalized by mean flow density, sonic speed, and reference length. The spatial derivation is calculated by fourth-order Dispersion Relation Preserving (DRP) scheme with seven-point stencil. This scheme makes it possible to minimize the dissipation and the dispersion error of numerical computation with appropriate stencil coefficients. In addition to this, damper of fourth-order is applied in each iteration to eliminate the nonphysical oscillation generated at the Cube boundary and the object boundary discussed below. Time integration is calculated by six-stage fourth-order Runge-Kutta scheme.

### 2.2 Computational algorithm

Computational mesh of BCM is generated by following procedures. Firstly, computational domain is divided into aggregation of square area named ‘‘Cube’’ as shown in Fig. 2. The difference of adjacent Cube size is the same or double. Each Cube is then divided by equi-spaced Cartesian mesh named ‘‘Cell’’ as shown in Fig. 3. Computation is performed in each Cube. In the method, all Cubes have the same number of Cells, so the load balance for parallel computation is equivalent and parallel efficiency is excellent. Each Cube has three fringe Cells (Fig. 3) overlapped with adjacent Cubes. With the help of the fringe Cells, fourth-order DRP scheme using seven-point stencil can be easily and accurately implemented in the whole area of computational domains. When mesh is locally refined, selected Cube for refinement is divided into four domains (Cubes), and each domain is sub-divided by prescribed Cells. In this procedure, computational domain is smoothed so that the size of adjacent Cubes is restricted to the same or double/half size. Figure 4 shows the computational algorithm employed in this research. At the beginning, mesh information, object shape and initial condition are given. In time integral, six sub-iterations constitute one timestep. In each iteration, all Cubes are parallelized using OpenMP. The procedures of computation in each Cube are summarized as follows:

- (1) Data exchange at Cube boundary
- (2) Computation of right hand side (R.H.S.) of the governing equations
- (3) Update of temporary physical quantities
- (4) Damping the pressure wave in absorbing domain

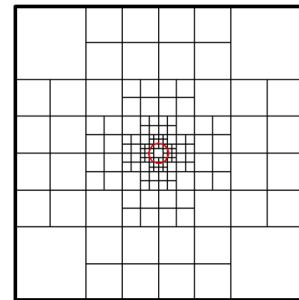


Fig. 2. Computational domain

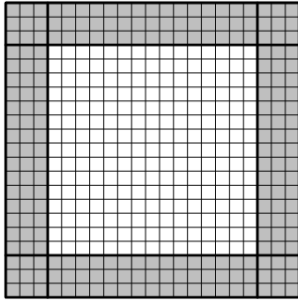


Fig. 3. Component of one Cube (15×15, 3Fringe Cell)

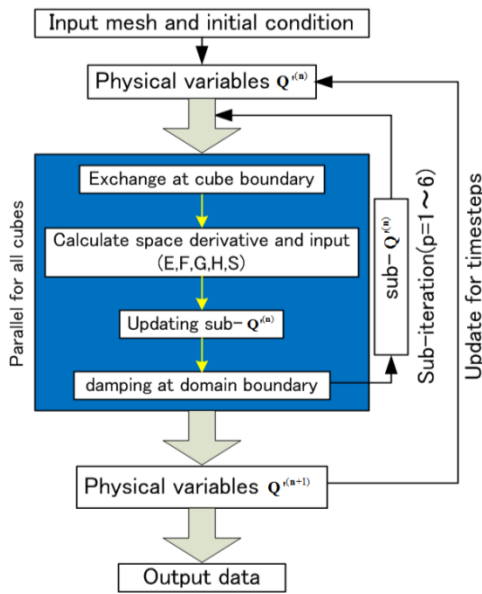


Fig. 4. Calculation algorithm

### 2.3 Wall boundary

At the computation by Cartesian mesh, the object surface is represented in a staircase pattern, but the real surface is smooth. Therefore, it is important to handle the effect of the object geometries in numerical way when treating the wall boundary of Cartesian mesh. It is also important that the computation follows the physical law. From these needs, many IBMs are proposed in various approaches and implementations. In this research, IBM using Ghost Cell and Image Point [4] is employed. Firstly, wall Cells adjacent to fluid Cells are defined as Ghost Cells. Secondly, Image Point is defined from Ghost Cell to the object's normal direction as shown in Fig. 5. In this process, the surface data which is used to determine the intersection point of normal vector with surface is STereo Lithography

(STL) data. Thirdly, physical quantities of Ghost Cells are calculated so that the velocity vector normal to the object is zero and the Neumann condition of pressure is satisfied. Interpolation to Image Point is conducted by inverse distance weighting method of Eq. (3) as in Fig. 6. If many stencils are used to interpolate the values of Image Point, the accuracy of interpolation may increase. However, large stencils area has the possibility to intersect with other area of object surface. Therefore,  $3 \times 3 \times 3 = 27$  points located out of the object are used in this study. The accuracy of wall boundary is raised by the refinement of meshes.

$$q_{IP} = \sum_{i=1}^{27} w_i q_i \times mask(i)$$

$$w_i = \frac{h_i^{-2}}{\sum_{j=1}^{27} h_j^{-2}} \quad (3)$$

$mask(i) = 1$ : fluid Cell

$mask(i) = 0$ : wall Cell

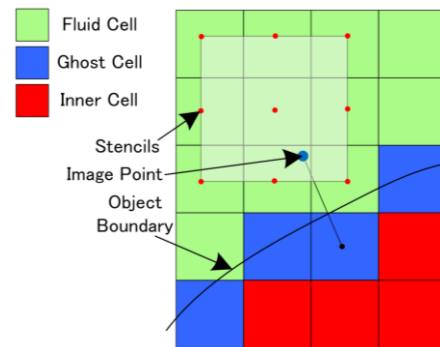


Fig. 5. Definition of Ghost Cell and Image Point

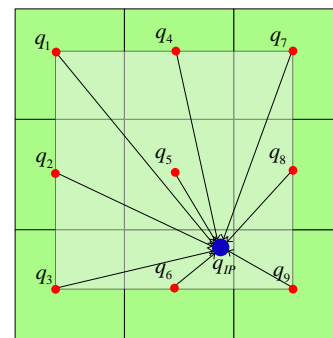


Fig. 6. Interpolation to Image Point

### 2.4 Cube boundary

At the boundary between Cubes with different sizes, three overlapping Cells are hanging nodes. Therefore, data exchange with high-order interpolation is needed. In this research, Lagrange interpolation is employed for data exchange at the boundary. This method calculates weighting functions as shown in Eqs. (4) and (5).

$$Q_{target}(x_{target}, y_{target}, z_{target}) = \sum_{j,k,l} Q_{surround.}(x_j, y_k, z_l) w_j(x_{target}) w_k(y_{target}) w_l(z_{target}) \quad (4)$$

$$w_j(x_{target}) = \prod_{i \neq j} \frac{(x_{target} - x_i)}{(x_j - x_i)} \quad (5)$$

$$w_k(y_{target}) = \prod_{i \neq k} \frac{(y_{target} - y_i)}{(y_k - y_i)}$$

$$w_l(z_{target}) = \prod_{i \neq l} \frac{(z_{target} - z_i)}{(z_l - z_i)}$$

Figure 7 shows stencils at the data exchange from small to large Cube in two-dimensional case. Interpolation to three overlapping Cells per one row is needed. Stencils of the Cell which is closest to boundary are  $2 \times 2 \times 2 = 8$  points and those of other two Cells are  $4 \times 4 \times 4 = 64$  points so that stencils are symmetric. Stencils of  $3 \times 3 \times 3 = 27$  points are used for four rows in three-dimension at the interpolation from large to small Cube (Fig. 8). This method is third-order of accuracy.

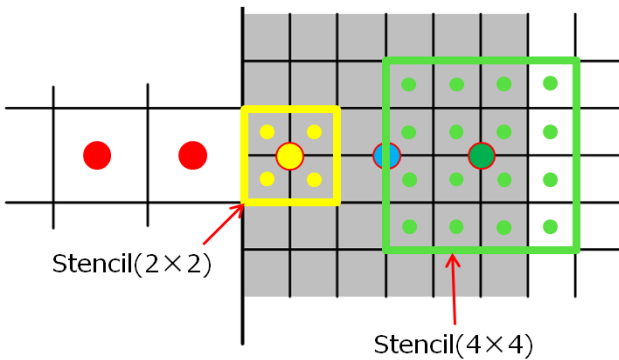


**Fig. 7. Interpolation from small to large Cube**

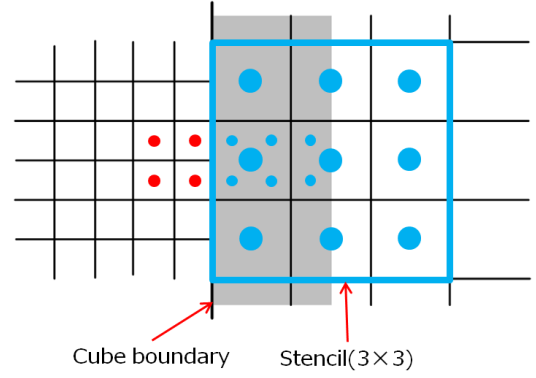


**Fig. 8. Interpolation from large to small Cube**

### 2.5 Absorbing boundary

In LEE computation, outgoing wave should be damped so that inner solution is not disturbed by reflected waves. In this research, the buffer zone boundary condition using the absorbing domain is implemented explicitly. To damp the outgoing wave accurately, the magnitude of damping coefficients varies as quadratic function of the coordinates toward the outer boundary. Maximum value is decided by minimum Cell size and speed of sound. Eqs. (6), (7), (8) show the damping equation in absorbing domain.

$$Q^{(n+1)} = \overline{Q^{(n+1)}} - \sigma \left( \overline{Q^{(n+1)}} - Q_{target} \right) \quad (6)$$

$$\sigma(x) = \sigma_{max} \left| 1 - \frac{x-L}{L} \right|^\beta$$

$$\sigma(y) = \sigma_{max} \left| 1 - \frac{y-L}{L} \right|^\beta \quad (7)$$

$$\sigma(z) = \sigma_{max} \left| 1 - \frac{z-L}{L} \right|^\beta$$

$$\sigma_{max} = \frac{2\bar{c}}{\Delta x}, \beta=2, Q_{target}=0 \quad (8)$$

In these equations,  $\sigma(x)$ ,  $\sigma(y)$ ,  $\sigma(z)$  are the damping coefficients of each direction, respectively.  $L$  is the width of absorbing domain.  $x$ ,  $y$ ,  $z$  are the distances from the inner boundary of domain.  $\overline{Q^{(n+1)}}$  is the solution computed after each iteration and  $Q_{target}$  is the target value to damp. Figure 9 shows the absorbing domain and close-up of bottom left corner in two-dimension.

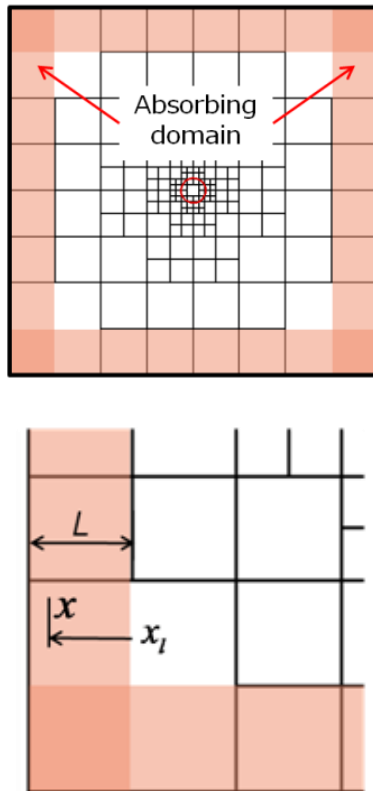


Fig. 9. Absorbing domain and close-up of bottom left corner

### 3 Noise scattering around fuselage-wing-nacelle configuration

Noise scattering around fuselage-wing-nacelle geometries of aircraft is simulated. As one of the configurations which achieve the large airport noise reduction, OWN configuration [5] that the engine nacelle is mounted over the wing is focused. The concept of this configuration is that the main wing shields engine noise toward ground. Therefore, the noise scattering around the full-geometry of DLR-F6 [6] and OWN is simulated and the far-field noise directivity is estimated. These configurations have complicated geometries and high curvature near the wing-body and the nacelle-pylon junctions. It is verified that the

present code has the capability to treat these complicated geometries in this computation. If the airplane is in real size, each length of airplane is supposed as in table 4. In the OWN configuration, nacelle is moved about 5.5m to  $x$  direction and about 3m to  $y$  direction from the location of DLR-F6. The pylon is used without change in geometry but has slope of 40 deg. As an example of modern turbofan engine, CFM56-7B engine is simulated. Bypass ratio is 5.5, fan diameter is 1.54m, number of blade is 24, maximum number of rotations is 5382rpm, and fundamental BPF is 2152.8Hz. This BPF is used as input frequency of spinning mode. The spinning mode  $(m,n)$  is set to  $(-24,0)$ . Maximum amplitude of fan noise is supposed to 300Pa and this is corresponding to about 143dB based on the reference sound pressure  $2.0 \times 10^{-5}$  Pa.

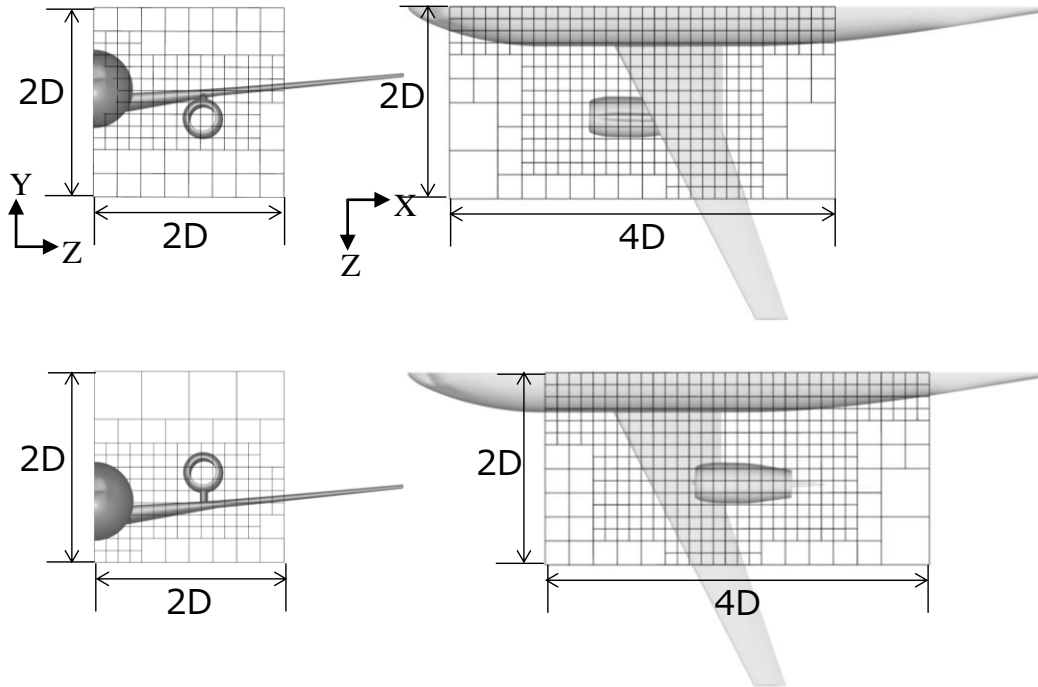
Table 5 shows the minimum Cell size, the number of Cubes, number of Cells in one Cube, the total number of Cells and the maximum PPW in each mesh. Figure 10 shows the computational domain of the each configuration. In this simulation, the reference length  $D$  is defined as the length of nacelle of longitudinal direction. The computational domains are  $4D \times 2D \times 2D$  and transferred to ensure that there are sufficient domains around the nacelle. In this process, it is supposed that the geometry out of computational domain doesn't have much effect for far-field noise directivity, thus only meshes in the computational domain are computed. The minimum Cell size is  $0.003125D$  and Cells of this size is located at the domain that needs to resolve the reflection and diffraction near the aircraft. Maximum PPW at meshes is 10.3. From the previous validation, PPW over twelve is needed to simulate with sufficient accuracy. Therefore the results have some errors. However, to validate the capability of treating the realistic geometries and to compare the far-field noise directivity between UWN and OWN are of interest.

Table 4. Dimension of each component

Fuselage length	32.5m
Nacelle length	4.9m
Nacelle diameter	1.5m
Fuselage diameter	4.2m

**Table 5. Mesh information**

	Min. Cell size	Number of Cubes	Number of Cells in one Cube	Total number of Cells	Point per wavelength
DLR-F6	0.003125D	3,299	40×40×40	211,136,000	10.3
OWN	0.003125D	3,432	40×40×40	219,648,000	10.3



**Fig. 10. Computational domain: DLR-F6 (upper) and OWN configuration (lower)**

Figure 11 shows the instantaneous pressure distribution at the cross-section surface of the nacelle center. This figure shows the whole domain including the absorbing domain. Noise from the nacelle propagates to the lateral direction and this noise is shielded by the main wing at the OWN configuration. Pressure history is monitored on the FW-H surface and the time convergence is observed at non-dimensional time  $T=15$ . Computational time is about three days in real time. Figure 12 shows the estimated SPL distribution at the 50m radius and its observing locations. In the real world, noise at the farther locations must be estimated. However, estimation of noise at farther location needs a huge amount of FW-H surface data. And also the linear propagation is assumed in the LEE computation. Therefore 50m distance is treated as far-field. In ICAO's rule, noise of airplane is determined by the noise level at the side and the bottom locations relative to the

fuselage. Therefore, noise distribution at the bottom of fuselage is estimated. From the figure, SPL of OWN configuration is lower by 10dB from 50deg. to 90deg. This is large noise reduction compared to the conventional aircraft. Mesh points on the FW-H surface is about 1.5 millions and 63 hundreds files are used to get the accurate solutions. Total size of data is about 280GB in double precision.

Figure 13 shows the logarithms of Prms of each object surface in Cartesian coordinate and Fig. 14 shows that value at the planes including the nacelle center. This value means the noise intensity. In Fig. 13, sound pressure from the inlet reaches the fuselage surface and generates the high noise intensity at the DLR-F6 configuration. On the other hand, higher pressure distribution on the main wing and fuselage surface can be seen. The noise from the nacelle inlet toward ground is effectively shielded by the main wing. Passages of noise

are clearly shown in Fig. 14. Figure 15 shows the SPL distribution on the fuselage surface at the coordinate of  $y=0.3$ , approximately corresponding to passenger seats. In the figure, the fringe pattern results from the interference

of noises from the inlet and the nacelle exit can be seen. At the OVN configuration, SPL from  $x=0.25$  to  $x=1.25$  is larger by about 10dB compared to that of DLR-F6. This would cause higher cabin noise.

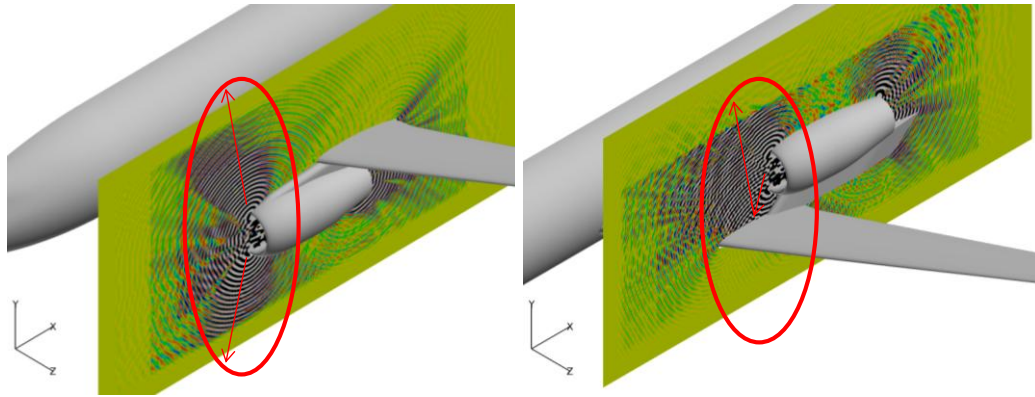


Fig. 11. Pressure distribution of UWN (left) and OVN (right)

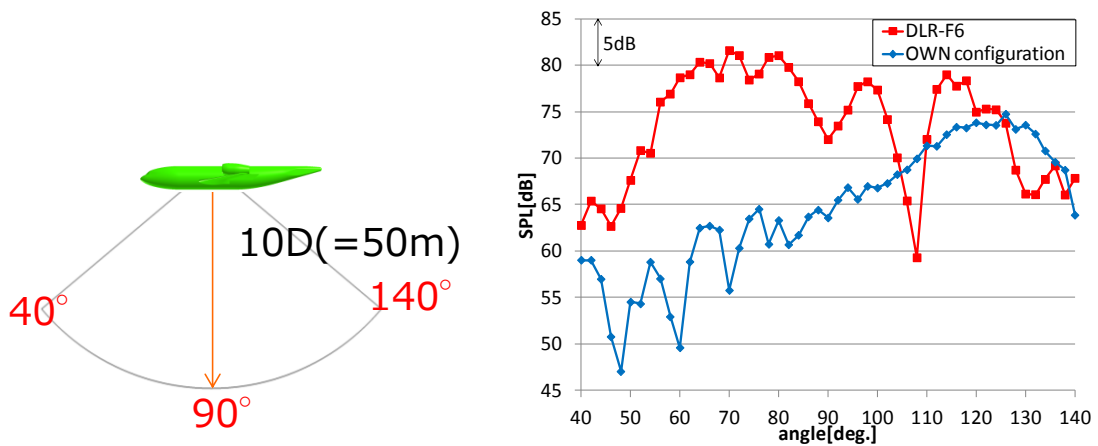
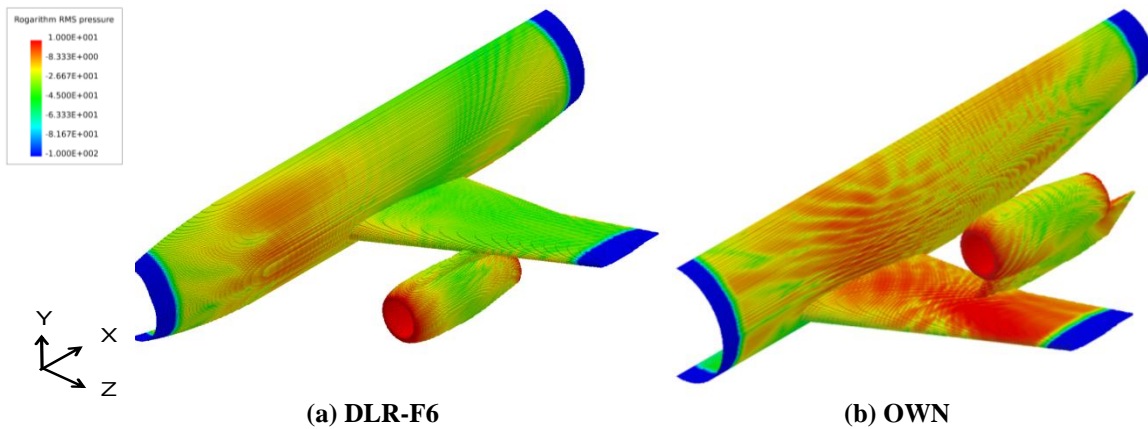
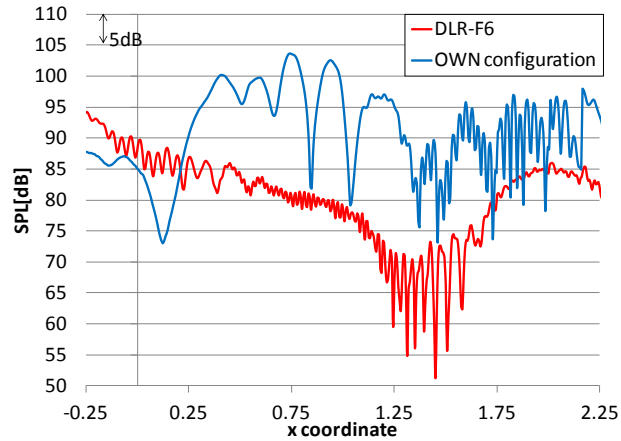
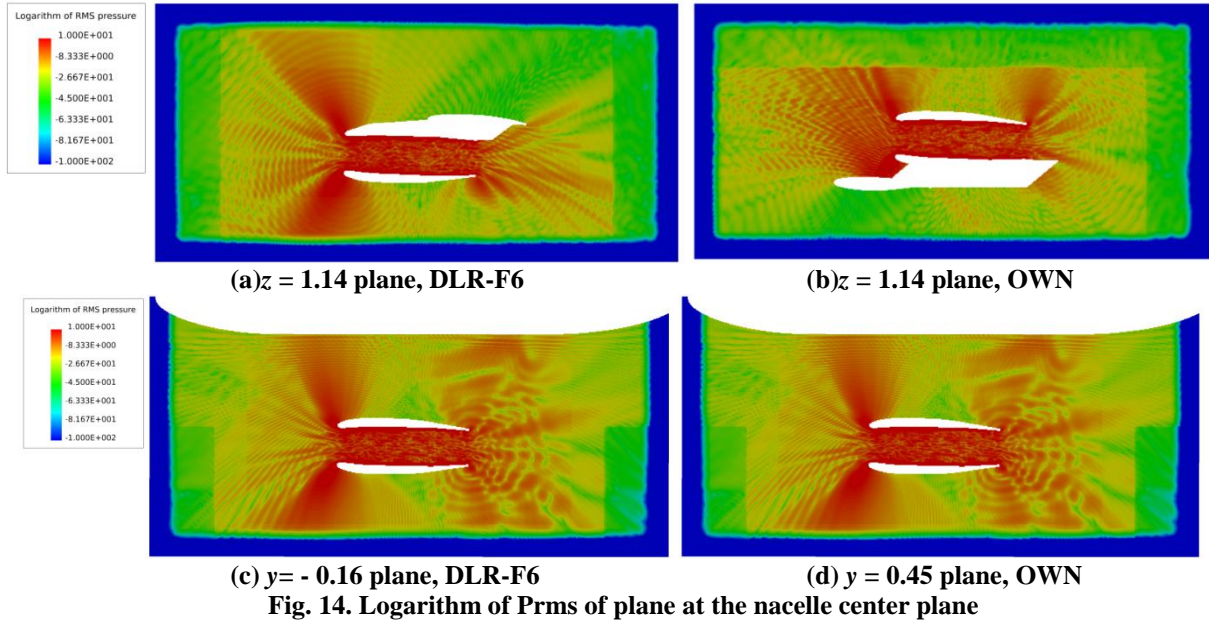


Fig. 12. Observing locations (left) and SPL distribution at 50m radius (right)



(a) DLR-F6 (b) OVN  
Fig. 13. Logarithm of Prms of object surface



#### 4 Conclusion

Noise scattering around a fuselage-wing-nacelle configuration was simulated and estimation of the noise shielding effect of OWN configuration is conducted. Aircraft configuration has complicated geometries especially near the wing-body and the nacelle-pylon junctions, and it was verified that the present code could treat these geometries. The total number of mesh points were about 200 million, and 280GB data were used to estimate the noise directivity at 50m radius. At the OWN configuration, the noise from the nacelle inlet was shielded effectively by the main wing because the noise diffracted strongly to the

lateral direction. SPL distribution of the OWN configuration at the far-field showed the 10dB lower values compared to that of conventional DLR-F6 configuration. The large noise shielding effect of OWN was proven. On the other hand, higher SPL value was determined at the fuselage surface of OWN relative to that of the DLR-F6, which would cause the higher cabin noise. The key to make OWN into the standard configuration of next generation is to find the solution reducing the cabin noise.

#### Acknowledgements

This work was supported by JSPS KAKENHI (21226018). The calculation in this

research was conducted by AltixUV1000 of Institute of Fluid Science, Tohoku University. The Ffowcs-Williams and Hawkings code using in this research is provided by Aviation Program Group of Japan Aerospace Exploration Agency (JAXA).

## References

- [1] Envia, E., “Emerging Community Noise Reduction Approaches,” 3rd AIAA Atmospheric Space Environments Conference, AIAA Paper 2011-3532, Jun. 2011.
- [2] Nakahashi, K. Kim, L-S., “High-Density Mesh Flow Computations by Building-Cube Method,” *Computational Fluid Dynamics 2004*, edited by C. Groth and D.W.Zingg, Springer, pp.121-126 (2006)
- [3] Nakahashi, K., “Building-Cube Method for Flow Problems with Broadband Characteristic Length,” *Computational Fluid Dynamics 2002*, Eds. S. Armfield, R. Morgan, K. Srinivas, Springer, 2003, pp.77-81.
- [4] Mittal, R., Dong, H., Bozkurtas, M., Najjar, F. M., Vargas, A., Loebbeche, von A., “A versatile sharp interface immersed boundary method for incompressible flows with complex boundaries,” *Journal of Computational Physics*. 227(2008)4827-4825.
- [5] Sasaki, D., Nakahashi, K., “Aerodynamic Optimization of an Over-the-Wing-Nacelle-Mount Configuration,” *Modeling and Simulation in Engineering*, vol. 2011, Article ID 293078, 13 pages, 2011. doi:10.1155/2011/293078
- [6] Laflin, K., *et al.* “Data Summary from the Second AIAA Computational Fluid Dynamics Drag Prediction Workshop,” *Journal of Aircraft*, vol. 42, No. 5, 2005, pp. 1165-1178.

## Copyright Statement

The authors confirm that they, and/or their company or organization, hold copyright on all of the original material included in this paper. The authors also confirm that they have obtained permission, from the copyright holder of any third party material included in this paper, to publish it as part of their paper. The authors confirm that they give permission, or have obtained permission from the copyright holder of this paper, for the publication and distribution of this paper as part of the ICAS2012 proceedings or as individual off-prints from the proceedings.